Editor invited article

A gradient regularized model for shape memory alloys

Hongrui Yu, Chad M. Landis *

Department of Aerospace Engineering and Engineering Mechanics and the Oden Institute for Computational Engineering and Science, The University of Texas at Austin, Austin, TX, USA

ARTICLE INFO

ABSTRACT

In this work a transformation strain gradient enhancement is introduced into a phenomenological constitutive model for the pseudoelastic behavior of shape memory alloys. The constitutive model is able to capture several unique features of the constitutive response of these materials during the transformation between austenite and martensite during the pseudoelastic response. These features include the asymmetry in the initial transformation stresses in tension versus compression, the asymmetry in the transformation strains in tension and compression, and finally the asymmetry in the hardening behavior in tension and compression. In fact, experiments have shown that untrained NiTi exhibits hardening during its transformation in compression, but softening for tensile loading. It is this softening behavior that motivates the need for the introduction of the transformation strain gradient into the constitutive modeling. Transformation strain gradient effects are introduced via a phase variable that describes the extent of transformation. The free energy of the material then depends on gradients of the phase variable, which introduces a material length scale into the theory. The governing equation for the phase variable is developed from a microforce balance and continuum thermodynamics analysis. The model is implemented in the commercial finite element software Abaqus through user defined subroutines and several numerical simulations are performed to illustrate the model response and lack of numerical mesh-dependency of the results.

1. Introduction

Shape memory alloys (SMAs) are a family of alloys that includes NiTi, CuAlNi, CuZnAl, AuCd and others, and they are best known for their shape memory effects and pseudoelastic behaviors (Lagoudas, 2008). These properties are enabled by the martensitic phase transformation between the austenite and martensite phases induced by stress or temperature change. SMA constitutive behaviors enable wide range of engineering applications in the aerospace, medical, automotive, and robotics areas. Although many of the above-mentioned alloys have their own advantage in specific applications, NiTi alloys are usually preferred due to their superior thermomechanical properties (Jani et al., 2014). Generally, the pseudoelastic behavior of SMAs is observed when the temperature is above the austenite finish temperature. The initial highly symmetric BCC lattice in the austenite phase becomes unstable under high stress, and transforms into the martensite phase that has a lower degree of symmetry. Once the applied stress is removed, the martensite becomes unsustainable, and transforms back to austenite (Shaw and Kyriakides, 1995).

Cisse et al. (2016) have reviewed the plethora of micromechanical and phenomenological models describing the pseudoelastic behavior of SMAs in existence. Most micromechanical models include the

variant volume fractions as internal variables. These models rely on micromechanical modeling to describe single grain behavior and the macroscopic polycrystalline material response is then obtained using homogenization, such as in Sun and Hwang (1993) Gall and Sehitoglu (1999) Boyd and Lagoudas (1996) and Berveiller et al. (1991), or through direct numerical simulation of grain structures, for example, in Gall et al. (2000) Anand and Gurtin (2003) Levitas and Ozsoy (2009) and Junker and Hackl (2011). These models produce detailed microstructural information but come with significant computational cost. As such, phenomenological models are more appropriate for the simulation of geometrically complex SMA structures. The first phenomenological model can be attributed to Tanaka and Nagaki (1982), and later Tanaka (1986) extended it to feature exponential transformation hardening functions. Many phenomenological models use an analogy to the classical theory of plasticity where transformation is governed by a transformation surface, hardening laws, and flow rules (Lagoudas et al., 1996; Souza et al., 1998), and its generalizations by Auricchio and Bonetti (2013), Scalet et al. (2019), and Alsawalhi and Landis (2022). More recent works on finite deformation include Xu et al. (2019) and Zhang and Baxevanis (2021), where

---

logarithmic strain is utilized to resolve spurious results arising from using non-integrable objective rates in the additive decomposition of the deformation gradient.

One important feature of SMA constitutive response is the asymmetry in the tensile and compressive behaviors. Experimental observations by Gall et al. (1999) and Bechle and Kyriakides (2014) both show the distinct behaviors of polycrystalline NiTi SMAs under tension versus compression. In order to accurately reproduce such asymmetry, Gall and Sehitoglu (1999) demonstrated the ability for a texture measurement coupled with a micromechanical model to predict the asymmetry. Peultier et al. (2008) and Frost et al. (2016) proposed models incorporating micromechanical information and introduced tension/compression asymmetry via a saturation function for the mean transformation strain. In contrast, Qidwai and Lagoudas (2000) use different types of phase transformation functions that enable tension/compression asymmetry and volumetric transformation. Each of these prior works utilizes the martensite volume fraction as an internal variable to describe the transformation state. Following the framework originally developed in Landis (2002, 2003a,b) for ferroelastic and ferroelectric switching behavior, Jiang and Landis (2016) proposed a phenomenological model for isothermal pseudoelastic SMA constitutive response that uses transformation strain as the sole internal variable. Instead of introducing tension/compression asymmetry through the transformation surface, this model uses a weighted mix of potentials that are calibrated to tensile and compressive responses. This feature allows the model to display hardening behavior in compression, and softening behavior in tension, as is observed in experiments.

Rate-independent phenomenological models with softening are susceptible to the issue of mesh-sensitivity or mesh-dependence of solutions due to the fact that sharp, zero thickness, boundaries form and propagate between large (transformed) and small (untransformed) deformation regions. Without a material length scale to regularize such boundaries, the governing mathematical problem becomes ill-posed. This issue can be addressed by introducing mild rate-dependency, as shown by Needleman (1988), or by including higher strain gradients as in He and Sun (2010), Duval et al. (2011), Rezaee Hajidehi and Stupkiewicz (2018). In He and Sun (2010), a macroscopic model for polycrystalline NiTi shape memory alloy is developed using a nonconvex strain energy density function along with a strain gradient term to account for the interfacial energy between different martensite and austenite phases. Both Duval et al. (2011) and Rezaee Hajidehi and Stupkiewicz (2018) introduce a nonlocal parameter that is coupled with its local counterpart through an additional partial differential equation that involves both the local and nonlocal parameter as well as the gradient of the nonlocal parameter. An internal material length scale is introduced through the additional PDE that limits the local instability.

In this paper, a gradient enhancement along the lines of Rezaee Hajidehi and Stupkiewicz (2018) is applied to the phenomenological constitutive model for pseudoelastic shape memory alloys of Jiang and Landis (2016). This model includes the definition of a transformation surface, an associated flow rule, and back-stresses defined through a transformation potential. Under this framework, the tension/compression asymmetry, and specifically the softening of the tensile response commonly observed in shape memory alloys can be captured, and the model is enhanced by a gradient regularization. Through the addition of a nonlocal phase variable that couples with equivalent transformation strain locally, and an energy penalty associated with its gradient, a material length-scale is introduced, thus eliminating artificial mesh-dependency. The model is implemented in the commercial software Abaqus through user defined subroutines to simulate the response of different structures under various loading scenarios. The first simulation performed is the uniaxial extension of a NiTi strip. The second simulation performed is on a stationary crack in a finite-sized specimen under mode-I loading conditions. Two crack tip locations are studied: one with the tip located at the center, while the other with the tip offset towards the edge. For each of these first

two geometries, a study is conducted to demonstrate the effect of the material length scale on the results. Finally, the uniaxial extension of a NiTi tube is simulated to demonstrate the capability of the model in three-dimensional applications.

The remainder of the paper is organized as follows: in the Formulation section, the main constitutive theory is presented in detail along with a derivation for the additional governing equation for the nonlocal phase variable; in the Finite Element Implementation section, the method of implementation as well as the simulation setups are briefly described and the simulation results and corresponding analyses are presented; finally, the theory and findings are summarized in the Summary section.

2. Formulation

In the following section, a gradient regularized phenomenological model for shape memory alloys is presented. Index notation will be utilized, and summation is implied over repeated indexes. Let σ_{ij} and ε_{ij} be components of the stress and strain tensor, respectively. The strain tensor is decomposed into elastic strain ε_{ij}^E and transformation strain $\varepsilon_{ij}^{\mathrm{T}}$ components. A scalar phase variable μ is introduced which describes the extend of transformation, such that $\mu = 0$ corresponds to no transformation and $\mu = \varepsilon_c$ corresponds to full transformation where ε_c is a material-specific parameter related to the saturation strain.

The following form of the Helmholtz free energy density function is assumed,

$$\psi(\varepsilon_{ij}, \varepsilon_{ij}^{\mathrm{T}}, \mu, \mu_{,i}) = \psi^E(\varepsilon_{ij}, \varepsilon_{ij}^{\mathrm{T}}) + \psi^{\mathrm{T}}(\varepsilon_{ij}^{\mathrm{T}}) + \psi^\mu(\mu, \varepsilon_{ij}^{\mathrm{T}}) + \psi^{Grad}(\mu_{,i}) \tag{1}$$

where

$$\psi^E = \frac{1}{2} C_{ijkl}(\varepsilon_{ij} - \varepsilon_{ij}^{\mathrm{T}})(\varepsilon_{kl} - \varepsilon_{kl}^{\mathrm{T}}) \tag{2}$$

$$\psi^\mu = \frac{1}{2} \kappa(\mu - \bar{\varepsilon}^{\mathrm{T}})^2 \tag{3}$$

$$\psi^{Grad} = \frac{1}{2} \kappa l_0^2 \frac{\partial \mu}{\partial x_i} \frac{\partial \mu}{\partial x_i} \tag{4}$$

Here, ψ^μ links the newly introduced phase variable μ to the equivalent transformation strain $\bar{\varepsilon}^{\mathrm{T}}$ (defined later in Eq. (22)), ψ^{Grad} introduces an energy penalty for the gradient of μ, ψ^E is the standard elastic free energy density, and ψ^{T} is the part of free energy density associated with the kinematic hardening model for transformation used for the derivation of back stresses. l_0 is the characteristic length scale of the material and κ is a penalty modulus. C_{ijkl} are components of the linear elastic stiffness tensor, which is assumed to be constant and isotropic in this study for the sake of simplicity.

To derive the governing equation for the phase variable μ, consider a body Ω and its enclosing boundary $\partial\Omega$ with outward unit normal $\boldsymbol{n}$. Introduce a set of external micro-forces: λ the surface micro-force per unit area, volume micro-force γ, and a set of internal micro-forces: π and ξ_i. Following the ideas outlined in Gurtin (1996), Fried and Gurtin (1993, 1994), the micro-force balance can be written as

$$\int_\Omega (\pi + \gamma) dV + \int_{\partial\Omega} \lambda dS = 0 \tag{5}$$

and

$$\lambda = \xi_i n_i \text{ on } \partial\Omega \tag{6}$$

Applying the divergence theorem and recognizing that the equality must be valid for any arbitrary volume, the point-wise form of the micro-force balance is obtained,

$$\xi_{i,i} + \pi + \gamma = 0 \tag{7}$$

The second law of thermodynamics for isothermal processes can be written as follows,

$$\int_\Omega \dot\psi dV \leq \int_{\partial\Omega} t_i v_i dA + \int_\Omega b_i v_i dV + \int_{\partial\Omega} \lambda \dot\mu dA + \int_\Omega \gamma \dot\mu dV \tag{8}$$

Again applying the divergence theorem and the arbitrary volume argument, the above inequality becomes

$$\left(\sigma_{ij} - \frac{\partial \psi}{\partial \varepsilon_{ij}}\right)\dot{\varepsilon}_{ij} + \left(\xi_{ij} - \frac{\partial \psi}{\partial \mu_{,i}}\right)\dot{\mu}_{,i} - \left(\pi_{ij} + \frac{\partial \psi}{\partial \mu}\right)\dot{\mu} - \frac{\partial \psi}{\partial \varepsilon_{ij}^{\mathrm{T}}}\dot{\varepsilon}_{ij}^{\mathrm{T}} \geq 0 \quad (9)$$

Following the Coleman–Noll procedure (Coleman and Noll, 1974), the first two terms are satisfied by

$$\sigma_{ij} = \frac{\partial \psi^E}{\partial \varepsilon_{ij}} = C_{ijkl}\left(\varepsilon_{kl} - \varepsilon_{kl}^{\mathrm{T}}\right) \quad (10)$$

$$\xi_i = \frac{\partial \psi^{\mathrm{Grad}}}{\partial \mu_{,i}} = \kappa l_0^2 \mu_{,i} \quad (11)$$

Then, by defining components of the backstress σ_{ij}^{B} as

$$\sigma_{ij}^{\mathrm{B}} = \frac{\partial \psi^{\mathrm{T}}}{\partial \varepsilon_{ij}^{\mathrm{T}}} + \frac{\partial \psi^{\mu}}{\partial \varepsilon_{ij}^{\mathrm{T}}} \quad (12)$$

The second law can be rewritten as

$$-\left(\pi + \frac{\partial \psi}{\partial \mu}\right)\dot{\mu} + \left(\sigma_{ij} - \sigma_{ij}^{\mathrm{B}}\right)\dot{\varepsilon}_{ij}^{\mathrm{T}} \geq 0 \quad (13)$$

This inequality will be satisfied in "strong form" by requiring that each term on the left-hand side satisfies the inequality independently of the other. The second term on the left-hand side will satisfy the inequality by assuming that no transformation strain evolves within a convex transformation surface that encloses the origin in $(\sigma_{ij} - \sigma_{ij}^{\mathrm{B}})$ space, and that transformation strain increments are normal to the transformation surface when $(\sigma_{ij} - \sigma_{ij}^{\mathrm{B}})$ is on the transformation surface. The first term on the left-hand side satisfies the inequality if,

$$\pi = -\frac{\partial \psi}{\partial \mu} - \beta\dot{\mu} \quad (14)$$

Taking the viscosity parameter β to be zero, then the governing equation for μ can be obtained from the micro-force balance as,

$$l_0^2 \mu_{,ii} + \bar{\varepsilon}^{\mathrm{T}} - \mu = 0 \quad (15)$$

where l_0 is the material-specific characteristic length-scale.

The following specific form of the kinematic hardening model is adopted for transformation strain evolution. The elastic states are enclosed by a Mises-type transformation surface defined by

$$\Phi^{\mathrm{T}} = \frac{3}{2}\left(s_{ij} - s_{ij}^{\mathrm{B}}\right)\left(s_{ij} - s_{ij}^{\mathrm{B}}\right) - \sigma_0^2 = 0 \quad (16)$$

where s_{ij} and s_{ij}^{B} are components of the deviatoric stress and back stress tensors, and σ_0 is the size of the transformation surface. The associated flow rule provides that the transformation strain increment is normal to the transformation surface and can be obtained as

$$\dot{\varepsilon}_{ij}^{\mathrm{T}} = \Lambda\left(s_{ij} - s_{ij}^{\mathrm{B}}\right) \quad (17)$$

Since Λ is constrained to be non-negative during transformation straining, it can be shown that

$$\left(\sigma_{ij} - \sigma_{ij}^{\mathrm{B}}\right)\dot{\varepsilon}_{ij}^{\mathrm{T}} = \Lambda\left(\sigma_{ij} - \sigma_{ij}^{\mathrm{B}}\right)\left(s_{ij} - s_{ij}^{\mathrm{B}}\right) = \frac{2}{3}\Lambda\sigma_0^2 \geq 0 \quad (18)$$

Hence the second law is satisfied.

The transformation potential is postulated to take the form of a weighted sum of tensile (t) and compressive (c) transformation potentials,

$$\psi^{\mathrm{T}} = \xi \psi_c^{\mathrm{T}} + (1-\xi)\psi_t^{\mathrm{T}} \quad (19)$$

where

$$\psi_t^{\mathrm{T}} = \underbrace{\left[\frac{H_{0t}J_2^{e2}}{2\varepsilon_c} + s_{1t}J_2^e + s_{1t}\varepsilon_{1t}\left(\exp\left(-\frac{J_2^e}{\varepsilon_{1t}}\right) - 1\right)\right]}_{\tilde{J}_t(J_2^e)}\underbrace{\left[\exp\left(\frac{m_t}{1-\bar{\varepsilon}^{\mathrm{T}}/\varepsilon_c}\right) + 1 - e^{2m_t}\right]}_{\tilde{E}_t(\bar{\varepsilon}^{\mathrm{T}})} \quad (20)$$
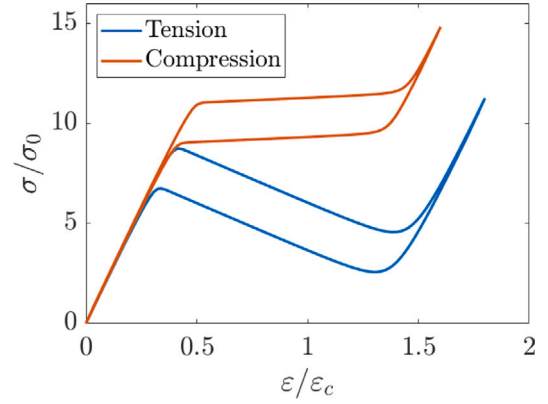

Fig. 1. Homogeneous uniaxial tension and compression stress–strain responses of an example material.

$$\psi_c^{\mathrm{T}} = \underbrace{\left[\frac{H_{0c}J_2^{e2}}{2\varepsilon_c} + s_{1c}J_2^e + s_{1c}\varepsilon_{1c}\left(\exp\left(-\frac{J_2^e}{\varepsilon_{1c}}\right) - 1\right)\right]}_{\tilde{J}_c(J_2^e)}\underbrace{\left[\exp\left(\frac{m_c}{1-\bar{\varepsilon}^{\mathrm{T}}/\varepsilon_c}\right) + 1 - e^{2m_c}\right]}_{\tilde{E}_c(\bar{\varepsilon}^{\mathrm{T}})} \quad (21)$$

with the following auxiliary definitions

$$J_2^e = \sqrt{\frac{2}{3}\varepsilon_{ij}^{\mathrm{T}}\varepsilon_{ij}^{\mathrm{T}}}, \quad J_3^e = \sqrt[3]{\frac{4}{3}\varepsilon_{ij}^{\mathrm{T}}\varepsilon_{jk}^{\mathrm{T}}\varepsilon_{ki}^{\mathrm{T}}},$$

$$\xi = \frac{f(J_3^e/J_2^e) - f(1)}{f(-1) - f(1)}, \quad \bar{\varepsilon}^{\mathrm{T}} = J_2^e f(J_3^e/J_2^e) \quad (22)$$

$$f(x) = \begin{cases} \left(\frac{\varepsilon_c}{\varepsilon_s} - 0.99\right)x^3 + 0.01x^6 + \frac{\varepsilon_c}{\varepsilon_s}, & x < 0 \\ \left(\frac{\varepsilon_c}{2\varepsilon_t} - 0.473\right)x^3 - 0.027x^6 + \left(\frac{1}{2}\left(\frac{\varepsilon_c}{\varepsilon_t} + 1\right) - \frac{\varepsilon_c}{\varepsilon_s}\right)x^{21} + \frac{\varepsilon_c}{\varepsilon_s} & x \geq 0 \end{cases} \quad (23)$$

This definition of transformation potential captures both strain and stress asymmetry between the tensile and compressive responses. The strain asymmetry is captured through the definition of the equivalent transformation strain in Eq. (22). This equivalent transformation strain variable maps any state of transformation strain onto a compressive state such that the transformation potentials dictate that strain saturation occurs as $\bar{\varepsilon}^{\mathrm{T}}$ approaches ε_c. Each potential is decomposed into a part, $\tilde{J}$, that solely depends on the J_2^e invariant of the transformation strain, and a part, $\tilde{E}$, that only depends on the equivalent transformation strain, $\bar{\varepsilon}^{\mathrm{T}}$. At small transformation strain levels, $\tilde{J}$ dominates and, since J_2^e remains the same for tension and compression, both responses remain similar. As the strain level increases, the effect of $\tilde{E}$ becomes more prominent. The equivalent transformation strain scales differently for tension and compression, thus producing different behaviors. Stress asymmetry is captured through the weight ξ, which mixes the uniaxial compression and tension behaviors for intermediate states, e.g. pure shear. When $\xi = 1$ uniaxial tension is recovered, and $\xi = 0$ represents uniaxial compression. The weighted sum of the tensile and compressive potentials then generalizes the uniaxial responses to arbitrary deformation states.

Note that each of the potentials can be calibrated individually to match independent tensile and compressive responses. The parameters H_0, ε_1, s_1, and m control the strength of the hardening/softening, the transition into the hardening/softening, the average stress level during transformation, and the onset of the saturation branch, respectively. An example of the stress–strain responses for uniaxial tension and
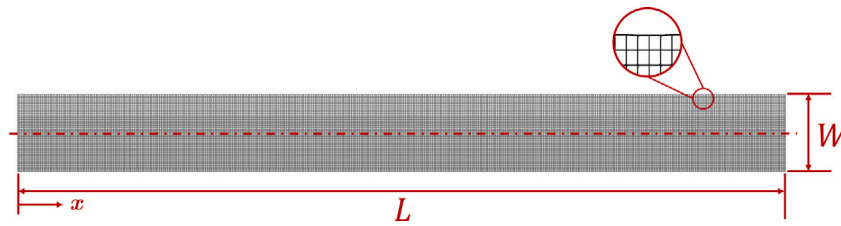
Fig. 2. Geometry of the model strip with the finite element mesh. The dashed line is the center-line of the strip where the phase parameter μ is presented in Figs. 5–7.

compression using the parameters reported in Table 1 are shown in Fig. 1.

3. Finite element implementation

Several numerical calculations are carried out to demonstrate the capability of the model. The model is implemented within the commercial finite element software Abaqus through user defined subroutines UMAT and HETVAL. Given the similarities between the governing equation for μ and that of a steady-state heat transfer problem, the analogy can be used such that the theory can be readily implemented using the existing coupled-temperature–displacement elements within Abaqus. It is noted that, as described in Seupel et al. (2018), there are difficulties with the Abaqus implementation if the "source" term, i.e., $(\bar{\varepsilon}^{\mathrm{T}} - \mu)$, is passed entirely through the "heat generation" variable in the UMAT subroutine. Therefore, the same split scheme as outlined in the afore-mentioned paper is used. Specifically, $\bar{\varepsilon}^{\mathrm{T}}$ is represented in HETVAL and $-\mu$ is passed through the UMAT's own heat generation variable. The rate of change of "heat generation" with respect to "temperature" is also handled through HETVAL. Since both parts of the "source" are recombined within the Abaqus solver, this split does not affect the simulation results.

3.1. Tension of a strip

Following the work of Jiang et al. (2017b), tension test simulations are performed on a strip with the dimensions $L : W = 10 : 1$ under plane strain conditions. The dashed line in Fig. 2 indicates the center line of the strip where representative distributions of the phase variable μ in the ensuing analyses will be presented in Figs. 5–7. In this simulation the axial and transverse displacements of all nodes on the left edge are zero, the transverse displacements on the right edge are zero, and the axial displacements on the right edge are all specified as δ. This case is denoted Case I and serves as a reference for comparison to different scenarios. The material length scale for Case I is $l_0 = l_1 = 9.1$ μm. The mesh consists of 64000 (80 along width and 800 along length direction) 4-noded linear plane strain coupled-temperature–displacement elements with reduced integration. In order to initiate localized transformation, a small geometric imperfection is introduced by means of a notch with 0.2% reduced width, positioned on the top of the strip approximately W away from the right edge. The material parameters used in this calculation are listed in Table 1.

A sequence of the strip in its deformed configuration along with normalized nominal stress and bending moment diagrams with bullet points corresponding to those of the deformation snapshots are presented in Fig. 3. The nominal stress is normalized by the size of transformation surface σ_0, and the bending moment is normalized by $M_0 = \sigma_0 W^2 / 6$.

The initial deformation of the strip up to Point 2 in Fig. 3(a) is for the most part uniform. Inhomogeneous deformation initiates close to the right end at an axial strain of approximately $0.4\varepsilon_c$. As shown in Image 2 in Fig. 3(c) (which corresponds to Point 2 on Fig. 3(a)), martensite transformation first appears as an inclined band close to the right end of the strip. Although there is only one visible band, the influence from a faint second characteristic band of the opposing

Table 1
Model parameters used for the strip tension simulations.

Parameter (unit)	Value	Parameter (unit)	Value
L (mm)	40.0	W (mm)	4.0
E (GPa)	68.1	σ_0 (MPa)	93.8
ν	0.425	ε_c (%)	3.3
l_1 (μm)	9.1	ε_s (%)	3.7
κ (GPa)	71	ε_t (%)	4.5
H_{0t} (GPa)	−11.4	s_{1t} (MPa)	750.4
H_{0c} (GPa)	1.4	s_{1c} (MPa)	938
m_t	0.001	ε_{1t} (%)	0.033
m_c	0.0001	ε_{1c} (%)	0.033

orientation produces a small kink in the angle of the boundaries of the primary band. The top of the leftward deformation front has an inclination of 42.3°, and the bottom of the leftward front has an inclination of 45.4°. The top of the right boundary of this deformation band has an inclination of 47.6° while the bottom of this side of the band has an inclination of 44.5°. In the nominal stress–strain behavior, the nucleation of the localized transformation bands coincides with a sharp drop in the average axial stress. The asymmetric propagation of the band contributes to a build-up of bending moments on the ends of the strip. As the transformation front propagates towards the left, the nominal stress level remains largely unchanged. At Point 3 in Fig. 3(a), the asymmetric front produces a kink in the upper boundary of the strip of around 1.3°. At this point, the faint second characteristic band is no longer actively influencing the austenite–martensite front, which is now a straight boundary with a slightly reduced inclination of 43.2°. A second band appears near the left end of the strip in the neighborhood of Point 4 in Fig. 3(a). Another thin stripe of martensite also nucleates from the bottom right corner of the strip and connects with the dominant transformation zone. As shown in Fig. 3(b), this results in some stabilization of the bending moments before they continue to increase between Points 5 and 8. The enlarged pictures show that the newly formed localization zones primarily follow the two characteristic band directions. The zone on the left expands slowly towards the dominant front and the two fronts eventually merge with each other as shown in Image 8 of Fig. 3(c), leaving a few islands of austenite material on either end of the strip. The merging of the transformation bands marks the maximum of bending moment during loading, and the nominal stress level starts to increase sharply. Aside from those at the very ends of the strip, the remaining small islands of austenite disappear at higher levels of displacement and the central region of the strip deforms uniformly until the end of loading phase.

The unloading behavior starting from Point 10 in Fig. 3(a) is quite different from what was observed during loading. As expected, the deformation is mostly homogeneous until Point 11. As seen in Image 11 in Fig. 3(c), the martensite to austenite transformation first occurs in the form of three distinct and symmetric islands at both ends of the strip. The three islands then break up into stripes with boundaries at the characteristic angles. Unlike martensite nucleation during loading, there is no significant change in either the nominal stress or the bending moment at Point 12 of Figs. 3(a) and (b). Throughout the majority of unloading, instead of a single propagating transformation front, both characteristics compete with one another, leaving a crisscross pattern
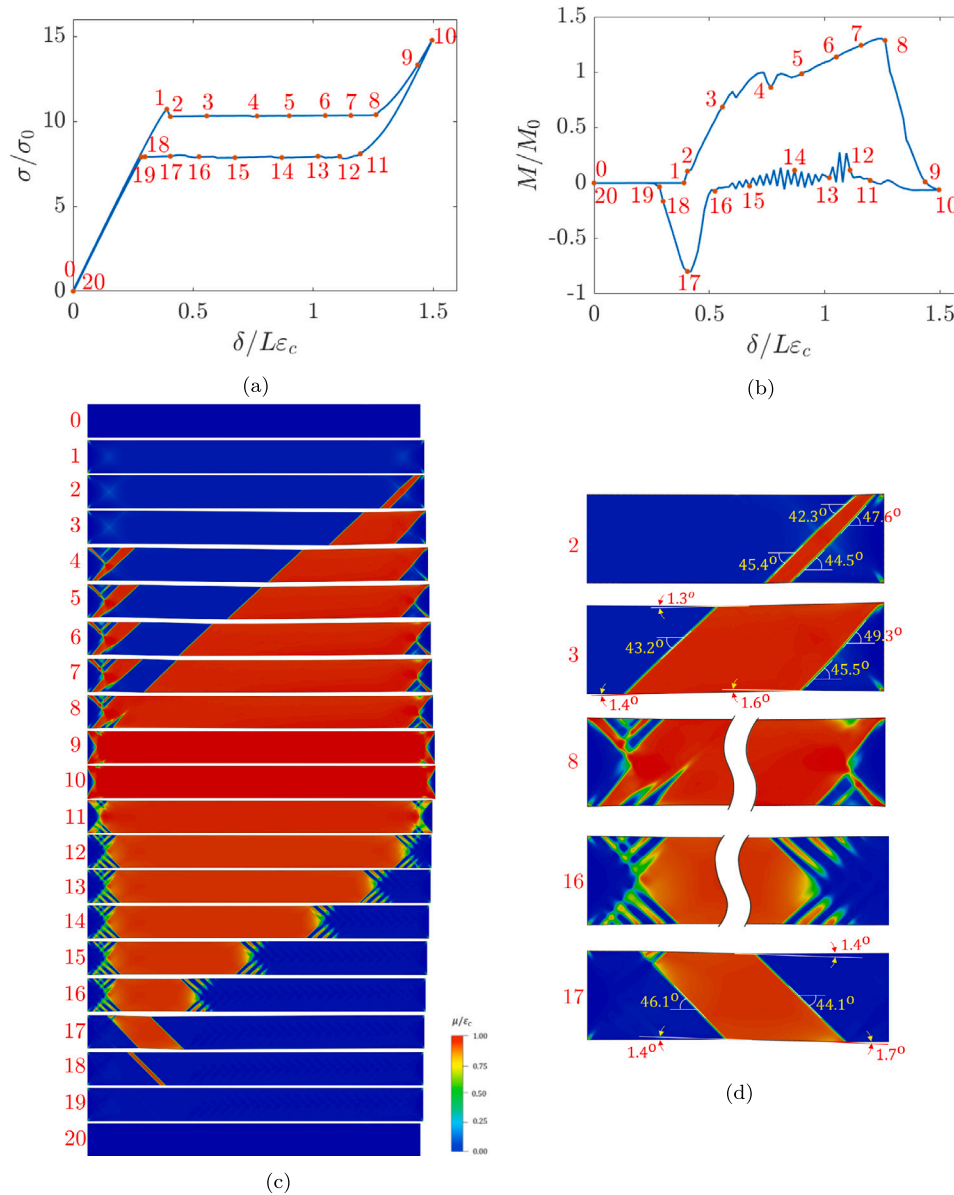
Fig. 3. The nominal stress–displacement curve for Case I; (b) The normalized bending moment–displacement curve for Case I; (c) Images of the strip in its deformed configuration for Case I with phase-field response μ superimposed corresponding to the Points in (a); (d) enlarged figure with details for select Images.

in their wake. The enlarged picture of Image 16 of Figs. 3(c) shows that the small martensite residual islands are mostly parallel to each other and align along the two characteristics. The nominal stress shows some small undulations but remains largely unchanged during this part of the behavior. However, the bending moment experiences significant oscillations due the evolution of the crisscrossed fingers on either side of the band. It is not until Point 17 in Fig. 3(a) that one of the characteristics finally becomes dominant and the fronts reduce to a single inclined band with boundaries at an inclination of around 44.1°. This produces a kink of 1.4° along the top boundary of the strip and 1.7° along the bottom. This asymmetry again leads to a sharp increase in the bending moment from Point 16 to Point 17 in Fig. 3(b). The moment then gradually drops as the single front retreats towards the left. After the band disappears around Point 19 of Fig. 3(a), the deformation again becomes mostly homogeneous while the stress drops to zero.

To study the effect of boundary conditions on the propagation of the transformation band, two additional simulations are performed with the same geometry and material parameters but different boundary

conditions. For Case II, the nodes at both ends are allowed to move freely in the transverse direction, except at the bottom-left corner where both displacement degrees of freedom are constrained to prohibit rigid body motions. As in Case I, the axial displacement on the left edge of the strip is set to zero, and all nodes on the right end are subject to a prescribed axial displacement δ. Case III is designed to allow for end rotation. The nodes on both the left and right ends are constrained to remain on a straight line that is allowed to rotate. The midpoints of each edge then serve as reference points for the relative displacement applied across the strip. The transverse displacements at both midpoints are set to zero, the left midpoint is fixed in the axial direction, and the axial displacement of the right midpoint is prescribed as δ.

As in the Case I, the average nominal stress in the axial direction is calculated and plotted against the prescribed displacement, normalized by $L\varepsilon_c$, as shown in Fig. 4(a)(b) for Case II and Case III, respectively, and normalized bending moment for both cases are plotted in Fig. 4(e). Sequences of the strips in their deformed configurations with contours of the phase variable superimposed are presented in Fig. 4(c)(d).
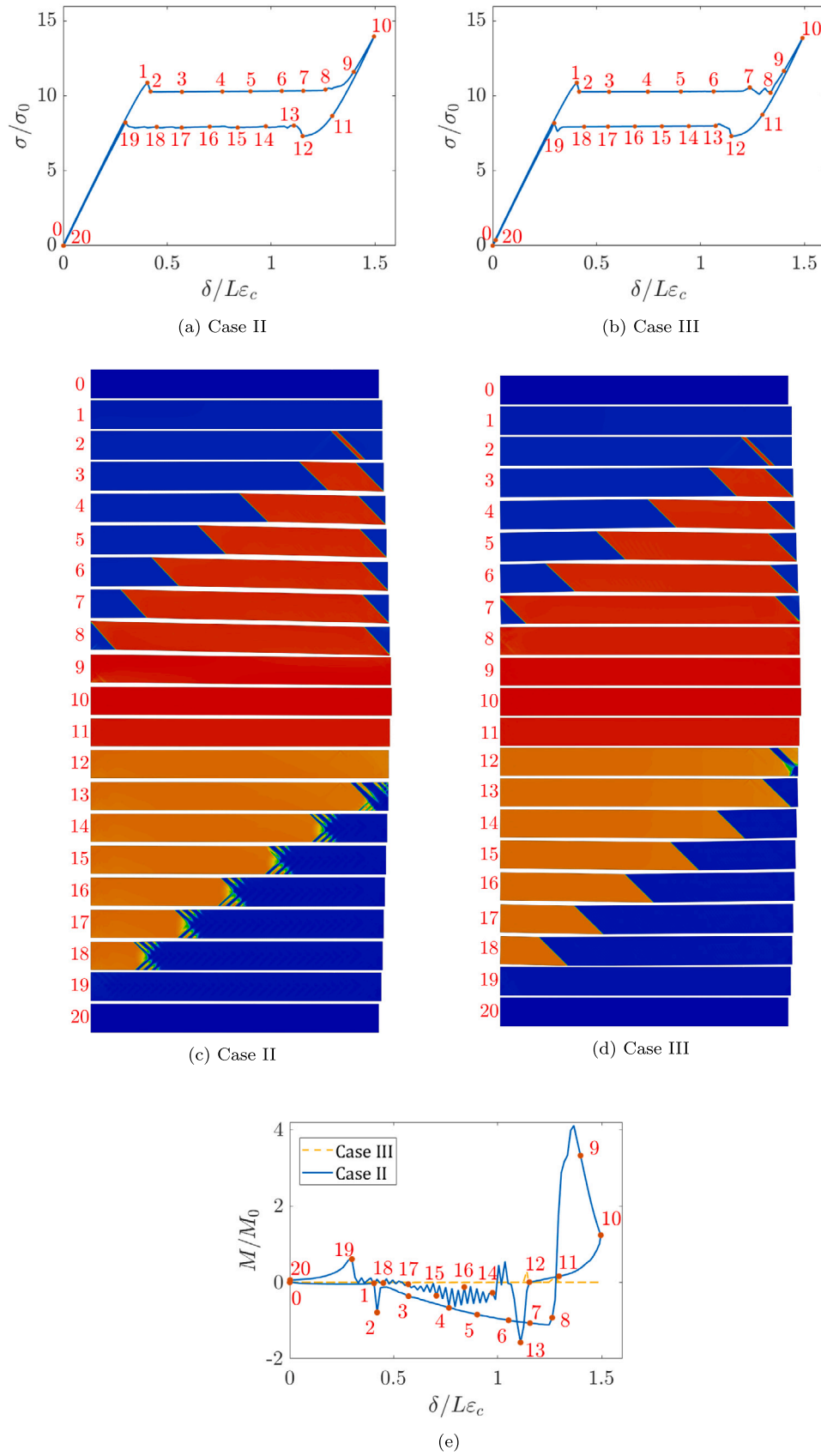
(a) Case II

(b) Case III

(c) Case II

(d) Case III

(e)

Fig. 4. (a)(b) Nominal stress–displacement curves for the strip tension test for Case II and III; (c)(d) Images of the calculated strip in its deformed configuration with the phase field variable μ superimposed corresponding to the Points in (a) and (b); (e) Normalized bending moment–displacement curves for Case II and III.

Table 2
Model parameters used for the different Cases in the parameter studies.

Parameter (unit)	Case I	Case IV	Case V	Case VI	Case VII
l_0 (μm)	9.1	18.3	36.6	9.1	9.1
H_{0t} (GPa)	−11.4	−11.4	−11.4	−14.25	−8.55
s_{1t} (MPa)	938	938	938	996	856

For both Case II and Case III, the loading behaviors are mostly identical. However, as shown in Fig. 4(e), due to the fact that boundaries in Case III are free to rotate, its bending moment is mostly negligible, while the bending moment for Case II exhibits a similar pattern as Case I. Homogeneous deformation persists until Point 2 in Fig. 4(a), where an inclined band of martensite transformation appears close to the right end of the strip. The front of the band then steadily propagates towards the left while the normalized nominal stress traverses a plateau. In the neighborhood of Point 8 in Fig. 4(a), the front reaches the end of the strip. The triangular austenite island is transformed between Points 8 and 9 while the stress starts to increase. Deformation becomes mostly homogeneous throughout the strip without any remaining austenite islands, in contrast to the case with fixed ends.

During unloading, the behaviors for Case II and Case III differ. For Case II, the reverse transformation nucleates in the form of several inclined stripes close to the right end of the specimen between Points 12 and 13 in Fig. 4(a). The nucleation corresponds to a jump in the stress–deflection curve. However, the transformation interface fails to maintain a preferred orientation and breaks up into a crisscross formation after Point 13, while the stress traverses a comparatively ragged plateau. Both characteristics compete with one another throughout the entire unloading phase. Unlike Case II, with the end being able to rotate, Case III exhibits only one characteristic during unloading. Although there is still a jump associated with nucleation of the band, the stress plateau is relatively flat compared to Case II.

3.2. Parameter study

In this section, the characteristic material length scale as well as tensile softening modulus are changed from Case I to study their effect on the propagation of transformation front. They are labeled Case IV through Case VII and the modified material parameters along with the reference parameters are listed in Table 2.

The gradient enhancement introduces a characteristic material length scale into the constitutive relation. In the following section, a brief parameter study is performed to demonstrate the effect of this length scale. The numerical simulation setup is identical to the fixed-boundary case, Case I, and material parameters are kept the same except for l_0. In addition to the original characteristic length of l_1, two additional cases with $2l_1$, denoted Case IV, and $4l_1$, denoted Case V, are simulated. The results are compared in Fig. 5.

In Fig. 5(a)(b) and (c), the sequences of the deformed strip with normalized phase variable response superimposed are presented for the cases of Case I, IV, and V, respectively. The load–deflection curves for these three cases are essentially identical to Fig. 3(a) and thus are not shown. The snapshots for Case IV and Case V are taken according to the bullet points used in Fig. 3. All three cases exhibit similar patterns during loading except that, for Case V, the band front is at the opposite inclination as for the other two cases. However, it is observed that the transition zones from the austenite to martensite regions differ in their sizes, with $4l_1$ having the widest transition zone and l_1 having the thinnest. To further illustrate this feature, the normalized phase variable distributions along the center line of the undeformed strips as shown in Fig. 2 at loading Point 3 in each case are plotted against relative horizontal distance Δx from the midpoint of the transition zone in Fig. 5(d) and (e). The front for the Case V spans about $83l_1$ and has the smoothest transition between the austenite and martensite regions.

The front spans across approximately $39l_1$ and $22l_1$ for Case IV and Case I, respectively. When the relative axial location is normalized by each respective characteristic length scale l_0, as in Fig. 5(e), all three curves coincide with each other indicating that the profile of the transition zone remain unchanged across different length scales and the actual width is scaled by the length-scale parameter l_0. During unloading, all three cases start with competing fronts at nucleation and transition to a single front near the end of unloading. With the smaller length-scales, the crisscross pattern is more pronounced. The pattern can be clearly observed with length-scales of $2l_1$ and l_1 while it is smeared out for the case of $4l_1$.

The next set of calculations illustrate the effect of the tensile softening modulus H_{0t}. Along with the softening modulus adopted in previous simulations, two additional cases with 20% stronger softening, denoted Case VI and 20% weaker softening, denoted Case VII, are examined. The parameter s_{1t} is adjusted accordingly to keep the average stress in the softening branch the same across all three cases. The other parameters remain unchanged. The new uniaxial tension stress–strain curves for these cases are plotted in Fig. 6(a). The resultant load deflection curves as well as a series of snapshots of the strips in their deformed configurations with the phase variable response superimposed are presented in Fig. 6(b), (c), (d), and (e), respectively.

The main features of the load deflection curves remain the same for all three cases with the only differences observed at the nucleation of the bands both during loading and unloading. At nucleation of the band during loading, a drop in nominal stress can be observed for both Case I and the greater softening Case VI. However, the transition into the stress plateau is relatively smooth for the low-softening Case VII. The mechanism for this smoothing can be seen at the onset of more diffused transformation bands at Point 1 of Fig. 6(e) before the full band nucleates. Other than this small detail, there are no significant differences in the load–deflection curves across these three cases.

As shown in Fig. 6(c), (d), and (e), the propagation patterns across all three cases are similar. However, the width of the transition zone between austenite and martensite regions varies slightly. Although not as prominent as the differences caused by a larger material length-scale l_0, the weaker softening modulus does produce a slightly wider transition zone, as evident in Fig. 6(f). This should not be unexpected since for a material that hardens any transitions between austenite and martensite should be smooth with little to no effect from the material length scale. The wider transition region for Case VII is more obvious during unloading, where the residual islands and crisscross pattern are clearly visible for Case VI and Case I, while these patterns are more diffuse in Case VII. The extent of the competing fronts during unloading also varies for different softening moduli. For Case VII, both characteristics persist until the very end of unloading and a glimpse of a single front can be observed in the neighborhood of Image 18 of Fig. 6(e). In comparison, for Case VI, the transition from dual characteristics to a single front happens earlier near Image 14 of Fig. 6(c).

3.3. Mesh sensitivity of the solution

The following simulations are performed with same set of parameters as in Case V where l_0 is set to 4 times the original value in Table 1 to allow for a wider front to facilitate this demonstration. A strip with the same dimensions as in the previous section is subjected to tension employing the fixed boundary conditions. Two additional mesh densities are compared with the one used in the previous sections. A coarser mesh with 400 elements along length and 40 along width (total 16000 elements, labeled $\frac{1}{4}N_0$), and a finer mesh with 1600 elements along length and 160 elements along width (total 256000 elements, labeled $4N_0$) are simulated. The snapshots of the front during propagation, as well as the results of the phase variable along the centerline of the strip are compared in Fig. 7. The overall simulation results are essentially the same as what has been observed and described in the previous demonstrations. To show that the results are independent of the mesh
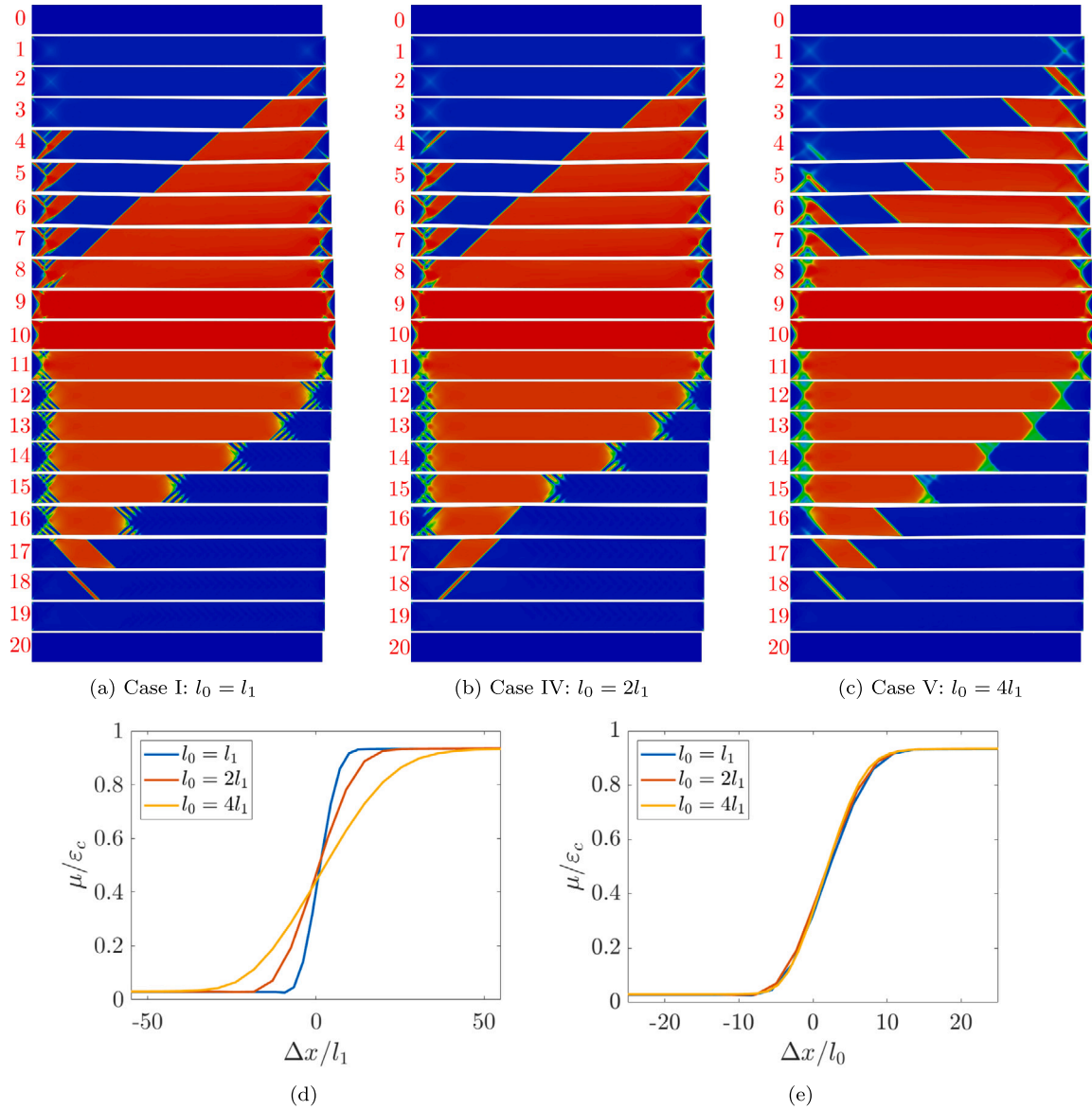
Fig. 5. (a) Sequence of the strip in its deformed configuration calculated using the original characteristic length l_1 (Case I); (b) sequence of the strip in its deformed configuration taken at bullet Points corresponding to those in the tensile test using $2l_1$ (Case IV); (c) sequence of the strip in its deformed configuration calculated using $4l_1$ (Case V); (d) normalized phase variable versus axial location normalized by l_1 across the center line of the strip for all three length-scales; (e) normalized phase variable μ versus axial location normalized by each respective l_0 across the center line of the strip for all three length-scales.

density, a snapshot of the strip with the phase variable superimposed is taken after one characteristic becomes dominant. In the enlarged snapshots, the transition zone spans multiple elements for each mesh density, and the width and shape of the transition zone remains the same. This is also evident in the $\mu/\varepsilon_c - x$ plot along the centerline around where the transition zone is located. In the plot, the phase variable changes from 0.1 in the region ahead of the front to around 0.9 in the region behind the front for all three cases. The transition zone is clearly visible and spans about 15 elements, 30 elements, and 60 elements, respectively for the $\frac{1}{4}N_0$, N_0, and $4N_0$ cases and there is no significant deviation within the three curves for the different mesh densities. This result clearly demonstrates that, with the introduction of the gradient regularization, mesh-sensitivity is eliminated. However, the mesh still needs to be fine enough to resolve the gradient of the phase variable, particularly on the boundary of the transition zone. As shown in Fig. 7(c), the same model but with meshes having only $\frac{1}{64}$ and $\frac{1}{128}$ of the original number of elements can generate mesh-dependent artifacts, such as the oscillation at the boundary of the

transition zone. The width of the transition zone also deviates slightly from the converged cases. For the simulations done in this paper, it is found that having 7 to 8 elements across the austenite to martensite transition zone is sufficient to generate consistent results, as seen in the $\frac{1}{16}N_0$ case.

3.4. Crack simulation

In this section, a mode-I crack opening simulation of a rectangular block with an edge crack is studied under plane strain conditions. Exploiting the symmetry of this problem, only the top half of the block is simulated, and the crack tip is assumed to be fixed (not growing). The geometry is shown in Fig. 8. Nodes located on the bottom edge to the right of the tip can only displace in the horizontal direction. A uniform and linearly increasing displacement is prescribed across the top of the block, and both the left and right edges of the block are traction free. The material parameters used in this set of simulations are the same as those used in Case I and outlined in Table 1. But the
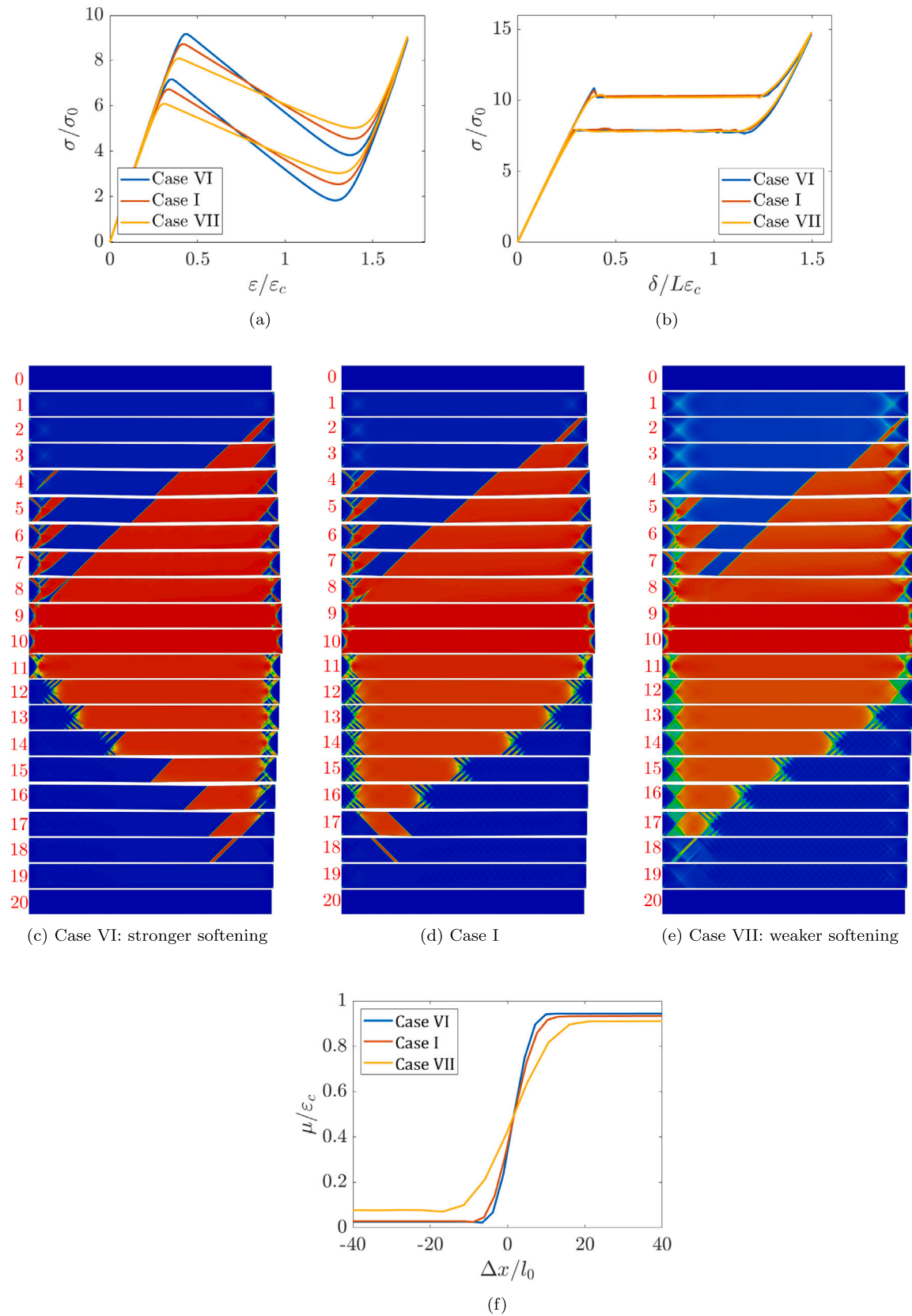
(a)

(b)

(c) Case VI: stronger softening

(d) Case I

(e) Case VII: weaker softening

(f)

Fig. 6. (a) Uniaxial stress–strain responses for each softening strength; (b) normalized nominal stress vs. normalized axial deflection of the strip; (c)(d)(e) the strip in its deformed configuration with the phase variable μ superimposed corresponding to +20% (Case VI, more softening), original (Case I), and −20% (Case VII, less softening) softening; (f) the normalized phase variable μ versus the axial location normalized by l_0 across the center line of the strip for all three softening cases.
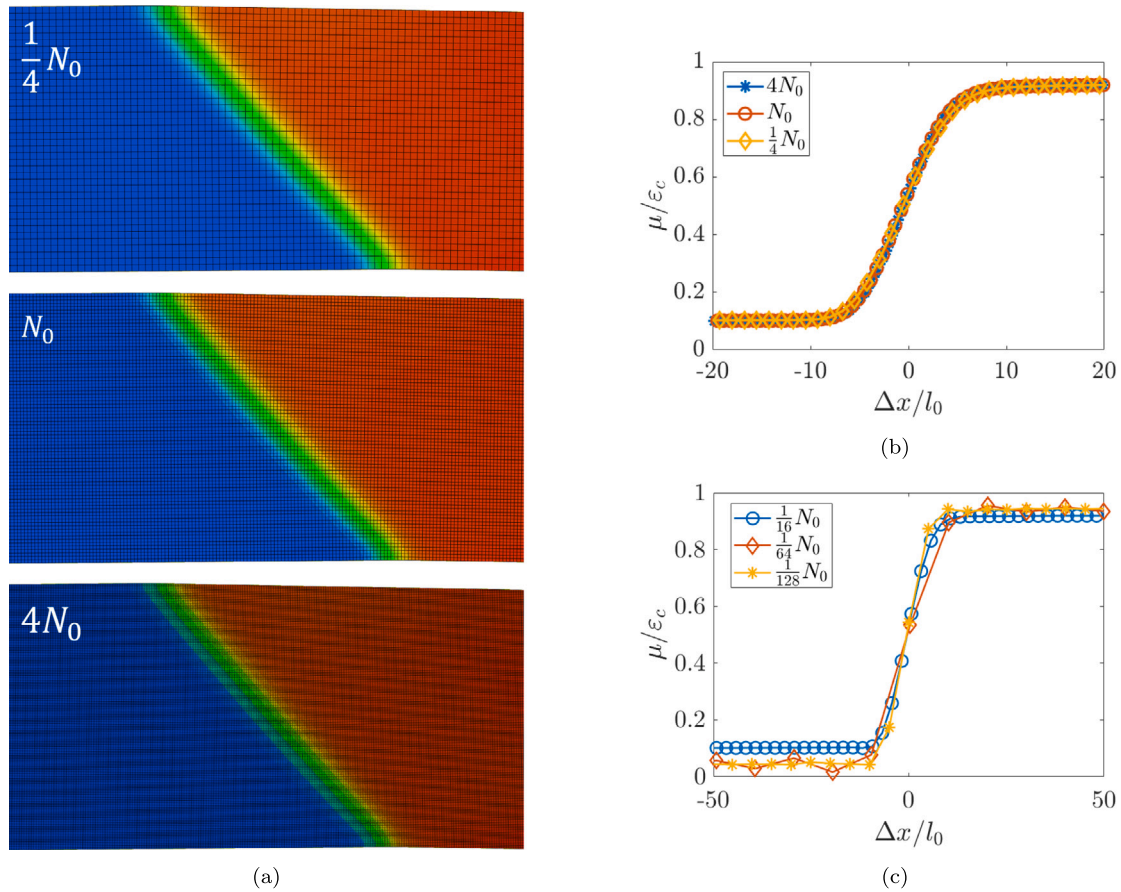
Fig. 7. (a) Enlarged views of the band transition zone for mesh densities of $\frac{1}{4}N_0$, N_0, and $4N_0$ during propagation; (b) normalized phase variable μ plotted along the centerline through the transition zone corresponding to the meshes shown in (a); (c) the normalized phase variable plotted along the centerline on coarser meshes.
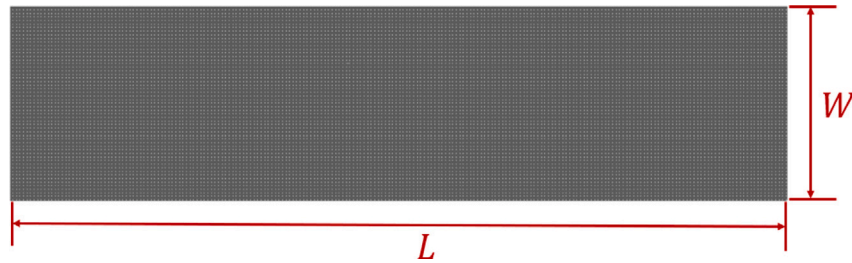

Fig. 8. Geometry of the crack model with the finite element mesh.

length, $L = 20$ mm, and width, $W = 5$ mm, are different. The material length scale is $l_0 = l_1 = 9.1$ μm.

First, the $L : W = 4 : 1$ rectangular block with the crack tip located at the center of the symmetry plane, $a = 0.5$ L, is studied. The mesh consists of 160000 uniformly distributed 4-noded bilinear coupled-temperature–displacement elements with reduced integration (CPE4RT). In Fig. 9(a), a normalized load–deflection ($F - \delta$) curve is presented during the loading phase. In Fig. 9(c), a set of 11 snapshots of the deformed block with contours of the phase-field distribution are presented corresponding to the numbered points on the load deflection curve.

It is seen that a small transformation region first occurs near the crack tip at Point 1 in Fig. 9(a). The localization then expands to form an inclined narrow ray at approximately 42° from the horizontal that extends from the tip towards the top edge. This also marks the start of a softer material response as seen in the load–deflection diagram. At Point 3 in Fig. 9(a), the ray intersects with the top edge and is reflected

at approximately −44° from the intersection point, forming an inverted V-shape. As the loading continues, the narrow band expands its width and additional rays start to appear at the same characteristic angles as the original set. In Image 5 of Fig. 9(c), one prominent ray initially at an angle of −134° appears on the left while another finger/strip appears parallel to the right branch. From this point on, additional rays continue to nucleate and the interaction between the two characteristics results in a crisscross pattern in the lower triangular region enclosed by the first two branches. At higher prescribed displacement levels, the individual martensite regions continue to expand and eventually merge with each other in the neighborhood of Point 9 in Fig. 9(a), from which point the material recovers its stiff response and the force increases sharply. There exists two small pockets of austenite material both ahead and behind the crack tip. While the pocket ahead of the tip will eventually transform at higher load, the one behind the tip remains untransformed even at high load levels. Next, the specimen with crack length $a = 0.2$ L is studied. The same mesh is used in this
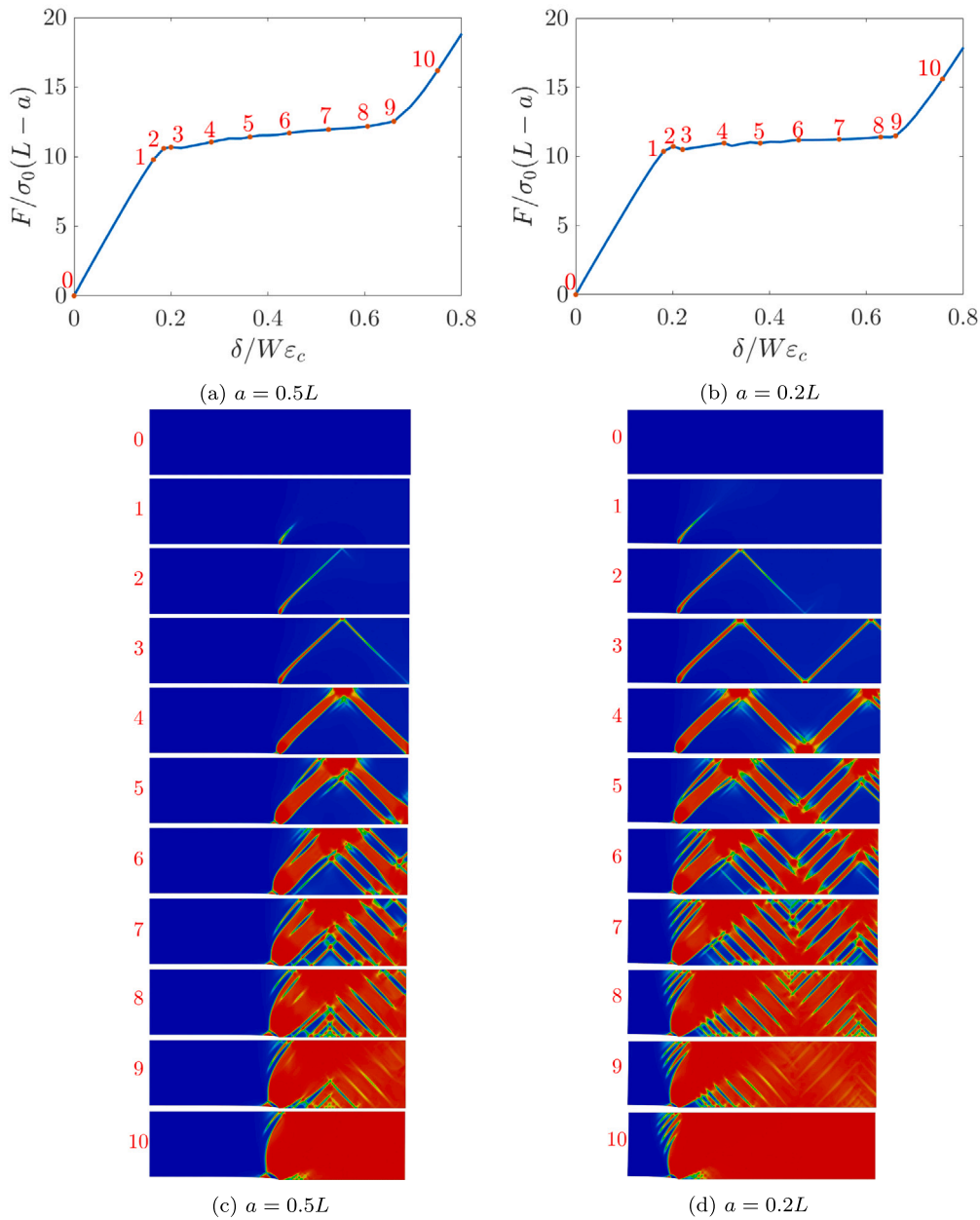
(a) $a = 0.5L$

(b) $a = 0.2L$

(c) $a = 0.5L$

(d) $a = 0.2L$

Fig. 9. (a) (c) Load–deflection curve for the case with centered crack tip, $a = 0.5$ L, and its corresponding sequence of the deformed configuration with μ superimposed; (b) (d) load–deflection curves for the case with the crack length at $a = 0.2$ L and its corresponding sequence of the deformed configuration with μ superimposed.

calculation and the normalized load–deflection curve as well as the corresponding deformed configurations with phase-field distributions superimposed are shown in Figs. 9(b) and (d). The transformation pattern is very similar to the results where the crack tip is located at the center. As in the center tip case, the localized bands initially form an inverted V-shape. the offset of crack tip provides more space for the pattern to continue through multiple reflections until it reaches the right edge of the block, forming a zigzag pattern. Again, at higher displacement levels, new branches parallel to the initial bands appear and interactions between the two characteristics produce crisscross patterns in the triangular regions enclosed by the initial branches. Most of the bands merge with one another in the neighborhood of Point 9 in Fig. 9(a), and the material resumes its stiff response. Again, in addition to the austenite pocket behind the tip that remains even higher loads,

there is also a small austenite island that does not fully transform just ahead of the crack tip.

The above simulations are also performed on the same geometry with the characteristic material length scale increased from its original setting, l_1, by a factor of 4 and 16, respectively. Fig. 10 presents the deformed configurations for both cases with phase-field distributions superimposed, along with the corresponding load–deflection curves. The main features for both load–deflection and transformation remain similar. In the deformed configurations for both scenarios, the increased material length scale produces a more diffuse transformation response, which is to be expected. The transformation differs from the original case more profoundly for $l_0 = 16l_1$. At Point 4 in Figs. 10(b), the two vertices are not connected by a strip of martensite material, as seen in both the $l_0 = l_1$ and $l_0 = 4l_1$ cases. Instead, the vertices continue
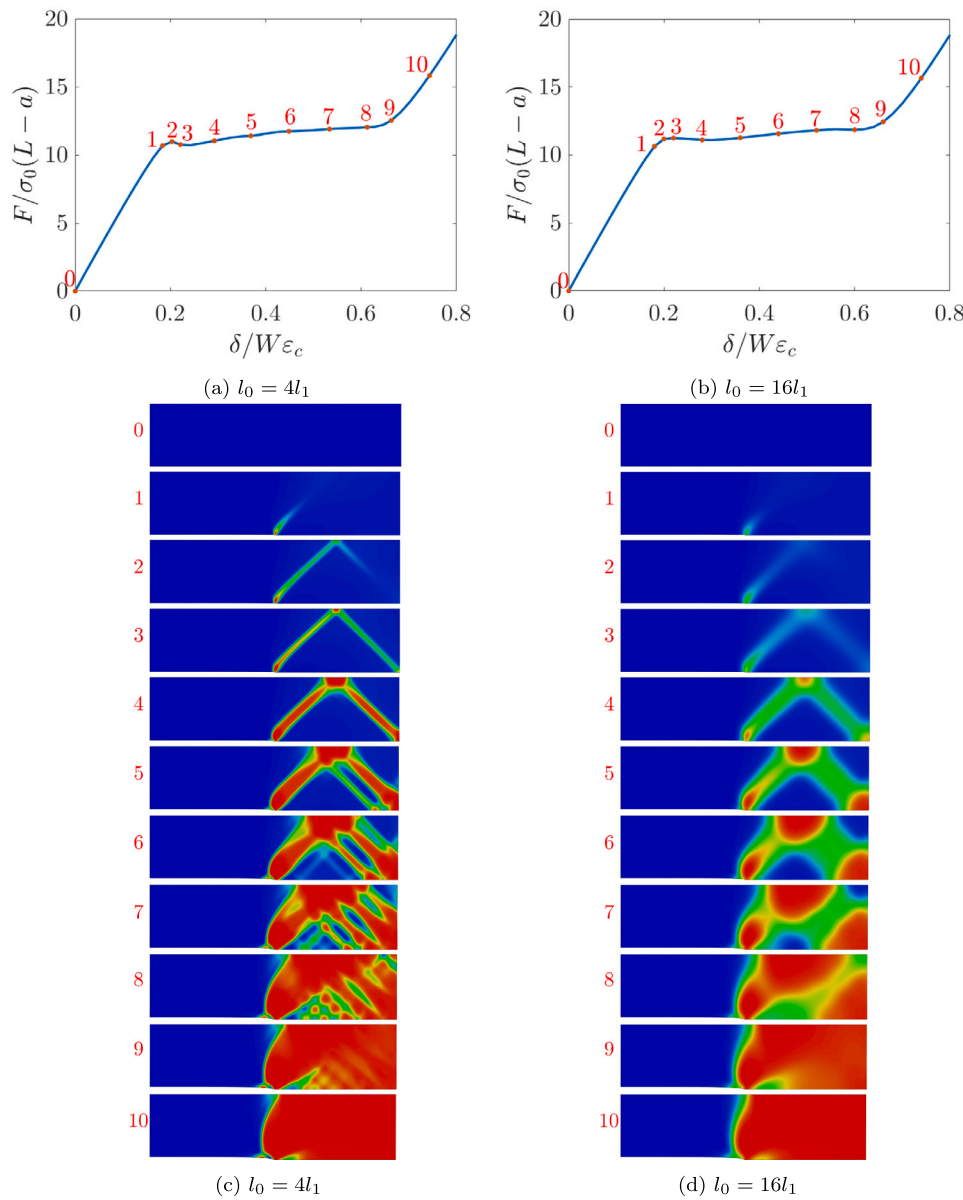
(a) $l_0 = 4l_1$

(b) $l_0 = 16l_1$

(c) $l_0 = 4l_1$

(d) $l_0 = 16l_1$

Fig. 10. (a) (c) Load–deflection curves for the case with a centered crack tip and the corresponding sequences of the deformed configuration with μ superimposed and material length-scale l_0 set to $4l_1$; (b) (d) Load–deflection curve for the case with center crack tip and its corresponding sequence of deformed configuration with phase-field superimposed and material length-scale l_0 set to $16l_1$.

to expand individually until they merge with one another. Once the regions merge, the force resumes its rapid ascent. There is essentially no austenite pocket behind the tip for the case with $l_0 = 16l_1$. But there still exists a pocket of austenite material ahead of the tip, which would transform at higher load level.

Crack calculations like these have the potential to be consequential for an experimental determination of the material length scale for a given material due to the interplay of length scales that exists in these problems. Specifically, there are three primary length scales, the material length scale associated with the austenite-to-martensite boundary of this theory, l_0, the size of the transformation zone near the crack tip under small-scale transformation assumptions, K_I^2/σ_T, and the specimen dimension which could be the crack length a, or in this case the height of the strip W. In problems where there is only hardening of the material, the material length scale l_0 will play no role and the size of the transformation zone will evolve from a shape that is governed by the stress intensity factor K_I and small-scale yielding considerations governed by the transformation stress σ_T, to

a large-scale yielding configuration that will alter the transformation zone due to interactions with the specimen geometry. However, when softening is introduced the material length scale plays a significant role in the transition from a small scale yielding transformation zone shape to the distinct bands that form and propagate. Additional studies of the instabilities that are triggered from the transformation zone in a softening material and how they are mediated by the material length scale l_0 are of interest, but left for future work.

3.5. Extension of a tube

In this final calculation, following the work of Jiang et al. (2017a), the constitutive model is implemented for the simulation of the axial extension of a NiTi tube. The geometry is shown in Fig. 11 and has dimensions $L = 10$ mm, $R = 2.5$ mm, and $t = 0.1$ mm. The material length scale is again $l_0 = l_1 = 9.1$ μm. In light of the results shown in Jiang et al. (2017a), where the phase transformation pattern evolves in a symmetric manner about the center plane, and
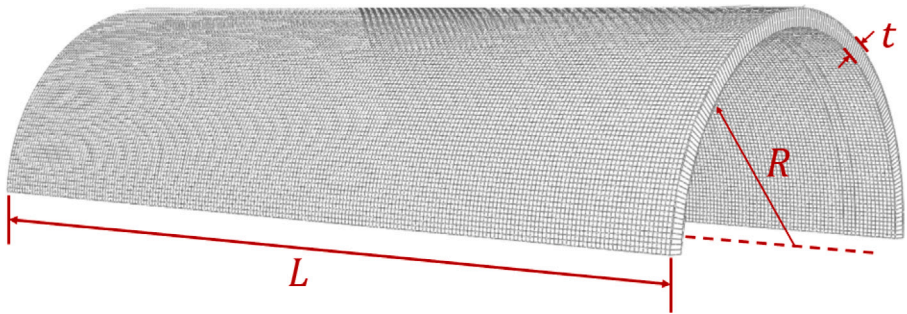
Fig. 11. Geometry of the model tube and the finite element mesh.
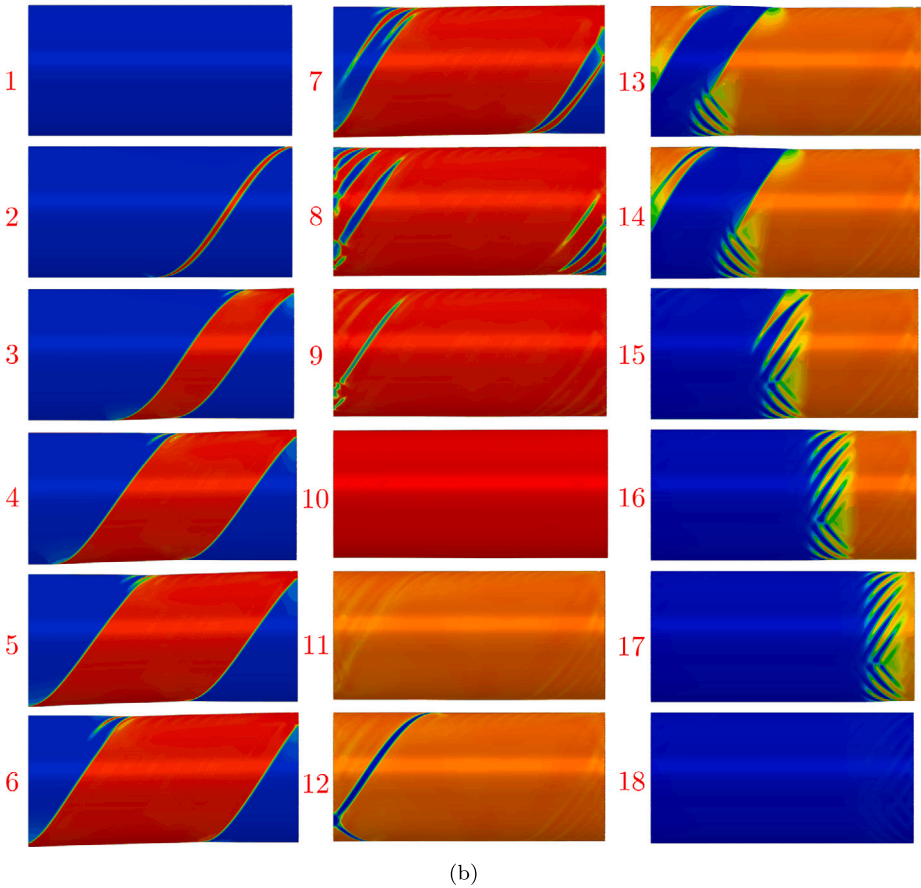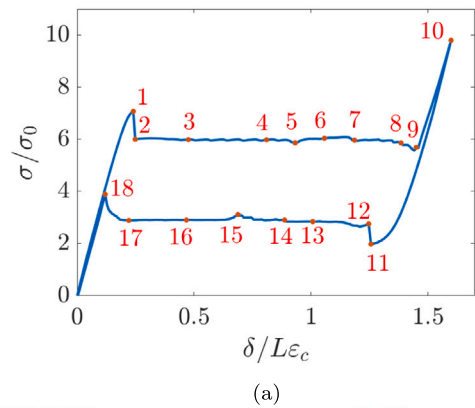

(a)

(b)

Fig. 12. (a) Average axial stress versus normalized elongation of the tube (b) Images of the deformed shape of the tube with normalized phase variable superimposed, corresponding to numbered bullet Points on the response shown in (a).

Table 3
Model parameters used for tension of a tube.

Parameter (unit)	Value	Parameter (unit)	Value
E (GPa)	80.1	σ_0 (MPa)	110.3
ν	0.425	ε_c (%)	3.3
l_0 (μm)	9.1	ε_s (%)	3.7
κ (GPa)	80.1	ε_t (%)	4.5
H_{0t} (GPa)	−4.76	s_{1t} (MPa)	418
H_{0c} (MPa)	66.8	s_{1c} (MPa)	572
m_t	0.001	ε_{1t} (%)	0.033
m_c	0.0001	ε_{1c} (%)	0.033

also to reduce computational cost, only half of the tube is modeled. The mesh consists of 194, 200, and 1 three-dimensional quadratic coupled-temperature–displacement elements along the circumference, length, and thickness directions, respectively. The axial displacement at one end is constrained to be zero and is prescribed at the other end. Symmetry conditions are prescribed along the symmetry plane. The tensile material parameters are calibrated to match that used in the experiment in Jiang et al. (2017a) and are shown below in Table 3.

The deformed shape of the tube with the normalized phase variable distribution superimposed is shown in Fig. 12(b), and the normalized average axial stress is plotted against normalized elongation of the tube in Fig. 12(a). The normalized average axial stress first experiences a nearly linear response before a sudden drop at Point 2 in Fig. 12(a), which corresponds to the nucleation of a thin spiral band originating from the corner of the tube, as evident in Image 2 of Fig. 12(b). The thin band forms an angle of approximately 55.7° with the symmetry plane and expands towards the fixed end of the tube. The asymmetric transformation causes a small kink angle at the interface between martensite and austenite materials. The transformation band front remains clean with the exception of a small region close to the symmetry plane, where short spikes of approximately the same angle as the main front can be observed. These short spikes become more prominent as the transformation front propagates. The main front stops its expansion when it reaches the fixed end at Point 5 in Fig. 12(a), while new spikes appear and fill the triangular gap near both ends. During propagation, the normalized average axial stress traverses a "bumpy" plateau between Points 2 and 9 in Fig. 12(a). The small undulations during this period can be attributed to the nucleation and merging of smaller spikes. Once the entire tube transforms to the martensite phase, the normalized average axial stress resumes its steep increase from Point 9 to 10 in Fig. 12(a).

During unloading, the deformation is again mostly uniform before the localized transformation bands first appear in the neighborhood of Points 11 and 12 in Fig. 12(a). A sharp increase in stress can be observed at Point 12 due to nucleation. The backward transformation first manifests as a thin band at approximately ±55.7° near the corner of the fixed end. As seen in Image 13 of Fig. 12(b), due to the interactions between the two characteristic angles, the front displays a crisscross pattern at one side near the symmetry plane while the other side remains mostly clean. This pattern cannot be sustained and, between Images 14 and 15 of Fig. 12(b), the inclined front breaks up into a multi-pronged formation with a base line that remains parallel to the ends of the tube and persists to the end of the retreat. The average stress increases between Point 17 and 18 in Fig. 12(a) when the transformation front reaches the end of the tube, followed by a monotonic drop while the tube undergoes uniform unloading.

4. Summary

A novel phenomenological model for pseudoelastic shape memory alloys with a gradient enhancement to regularize martensite to austenite transition zones in strain softening materials is introduced. By introducing a new phase variable that couples with the equivalent transformation strain, a material length scale is introduced to eliminate artificial mesh dependency. The model is implemented within the finite element method, and several numerical calculations were carried out to illustrate the behaviors of the model.

In the simulations of the extension of NiTi strips, the model successfully produces the inhomogeneous response commonly observed in NiTi under uniaxial tension. The load–deflection curve exhibits the typical plateau during transformation. The effect of boundary conditions on the characteristics of the Lüders-like band front were studied and discussed. It was shown that the restriction on rotation of the ends of the strip inhibit the propagation of a single front, which is more often seen in experiments. The material length scale is one of the key features in this constitutive model, which controls the width of the transition zone between the transformed and untransformed material. A comparison of results for different mesh densities was performed to illustrate the lack of mesh dependency of the solutions. The phase variable results along the centerline for each mesh density that sufficiently resolves the material length scale each agree with one another, indicating no artificial mesh-dependence exists in the numerical solutions. It was also shown that the length scale has a relatively small impact on the overall load–deflection behaviors of the structures studied.

The second set of calculations modeled the evolution of transformation emanating from a crack loaded in mode-I. In these simulations, interesting patterns of transformation develop. As expected, the transformation first occurs near the crack tip, but thereafter an inclined narrow band of transformed material originating from the tip develops and extends towards the top edge of the specimen, unlike what happens in a strain hardening material. The band then "reflects" off of the top surface of the specimen and again from the symmetry plane if there is enough space to do so in the horizontal direction. Once the primary zig-zag band structure is established, further deformation causes new bands to emerge from these while the primary bands widen. Ultimately a complex microstructure develops and evolves until much of the region ahead of the crack has transformed to martensite. The interest in these crack calculations stems from the fact that they may play a role in determining the material length scale experimentally. The interplay between the material length scale, the transformation zone size, and the specimen size presents the opportunity to compare experimental observations of the microstructures that develop in softening materials to the numerical simulations with the material length scale that produces the same details of the microstructures.

Lastly, uniaxial extension of a NiTi tube is simulated. The results of this three-dimensional simulation agrees with the prior experimental and numerical observations on tubes. However, the prior numerical simulations used the mesh size to regularize the austenite–martensite interface width, while the present simulations are mesh-independent. These results demonstrate that the proposed constitutive model is able to accurately reproduce three-dimensional structural instabilities.

Declaration of competing interest

Data availability

Data will be made available on request.

Acknowledgment

References

Alsawalhi, M.Y., Landis, C.M., 2022. A new phenomenological model for shape memory alloys. Int. J. Solids Struct. 257, 111264.

Anand, L., Gurtin, M.E., 2003. Thermal effects in the superelasticity of crystalline shape-memory materials. J. Mech. Phys. Solids 51 (6), 1015–1058.

Auricchio, F., Bonetti, E., 2013. A new "flexible" 3D macroscopic model for shape memory alloys. Discrete Contin. Dyn. Syst.-S 6 (2), 277.

Bechle, N.J., Kyriakides, S., 2014. Localization in NiTi tubes under bending. Int. J. Solids Struct. 51 (5), 967–980.

Berveiller, M., Patoor, E., Buisson, M., 1991. Thermomechanical constitutive equations for shape memory alloys. Le Journal de Physique IV 1 (C4), C4–387.

Boyd, J.G., Lagoudas, D.C., 1996. A thermodynamical constitutive model for shape memory materials. Part I. The monolithic shape memory alloy. Int. J. Plast. 12 (6), 805–842.

Cisse, C., Zaki, W., Ben Zineb, T., 2016. A review of constitutive models and modeling techniques for shape memory alloys. Int. J. Plast. 76, 244–284.

Coleman, B.D., Noll, W., 1974. The thermodynamics of elastic materials with heat conduction and viscosity. In: The Foundations of Mechanics and Thermodynamics. Springer, pp. 145–156.

Duval, A., Haboussi, M., Ben Zineb, T., 2011. Modelling of localization and propagation of phase transformation in superelastic SMA by a gradient nonlocal approach. Int. J. Solids Struct. 48 (13), 1879–1893.

Fried, E., Gurtin, M., 1993. Continuum theory of thermally induced phase transitions based on an order parameter. Physica D 68 (3), 326–343.

Fried, E., Gurtin, M., 1994. Dynamic solid-solid transitions with phase characterized by an order parameter. Physica D 72 (4), 287–308.

Frost, M., Benešová, B., Sedlák, P., 2016. A microscopically motivated constitutive model for shape memory alloys: formulation, analysis and computations. Math. Mech. Solids 21 (3), 358–382.

Gall, K., Lim, T.J., McDowell, D.L., Sehitoglu, H., Chumlyakov, Y.I., 2000. The role of intergranular constraint on the stress-induced martensitic transformation in textured polycrystalline NiTi. Int. J. Plast. 16 (10–11), 1189–1214.

Gall, K., Sehitoglu, H., 1999. The role of texture in tension–compression asymmetry in polycrystalline NiTi. Int. J. Plast. 15 (1), 69–92.

Gall, K., Sehitoglu, H., Chumlyakov, Y.I., Kireeva, I., 1999. Tension–compression asymmetry of the stress–strain response in aged single crystal and polycrystalline NiTi. Acta Mater. 47 (4), 1203–1217.

Gurtin, M.E., 1996. Generalized Ginzburg-Landau and Cahn-Hilliard equations based on a microforce balance. Physica D 92 (3–4), 178–192.

He, Y.J., Sun, Q.P., 2010. Macroscopic equilibrium domain structure and geometric compatibility in elastic phase transition of thin plates. Int. J. Mech. Sci. 52 (2), 198–211.

Jani, J.M., Leary, M., Subic, A., Gibson, M.A., 2014. A review of shape memory alloy research, applications and opportunities. Mater. Des. (1980-2015) 56, 1078–1113.

Jiang, D., Kyriakides, S., Landis, C.M., 2017a. Propagation of phase transformation fronts in pseudoelastic NiTi tubes under uniaxial tension. Extreme Mech. Lett. 15, 113–121.

Jiang, D., Kyriakides, S., Landis, C.M., Kazinakis, K., 2017b. Modeling of propagation of phase transformation fronts in NiTi under uniaxial tension. Eur. J. Mech. A Solids 64, 131–142.

Jiang, D., Landis, C.M., 2016. A constitutive model for isothermal pseudoelasticity coupled with plasticity. Shape Memory Superelast. 2 (4), 360–370.

Junker, P., Hackl, K., 2011. Finite element simulations of poly-crystalline shape memory alloys based on a micromechanical model. Comput. Mech. 47 (5), 505–517.

Lagoudas, D.C., 2008. Shape Memory Alloys: Modeling and Engineering Applications. Springer.

Lagoudas, D.C., Bo, Z., Qidwai, M.A., 1996. A unified thermodynamic constitutive model for SMA and finite element analysis of active metal matrix composites. Mech. Compos. Mater. Struct. 3 (2), 153–179.

Landis, C.M., 2002. Fully coupled, multi-axial, symmetric constitutive laws for polycrystalline ferroelectric ceramics. J. Mech. Phys. Solids 50 (1), 127–152.

Landis, C.M., 2003a. On the fracture toughness of ferroelastic materials. J. Mech. Phys. Solids 51 (8), 1347–1369.

Landis, C.M., 2003b. On the strain saturation conditions for polycrystalline ferroelastic materials. J. Appl. Mech. 70 (4), 470–478.

Levitas, V.I., Ozsoy, I.B., 2009. Micromechanical modeling of stress-induced phase transformations. Part 2. Computational algorithms and examples. Int. J. Plast. 25 (3), 546–583.

Needleman, A., 1988. Material rate dependence and mesh sensitivity in localization problems. Comput. Methods Appl. Mech. Engrg. 67 (1), 69–85.

Peultier, B., Ben Zineb, T., Patoor, E., 2008. A simplified micromechanical constitutive law adapted to the design of shape memory applications by finite element methods. Mater. Sci. Eng. A 481, 384–388.

Qidwai, M., Lagoudas, D., 2000. On thermomechanics and transformation surfaces of polycrystalline NiTi shape memory alloy material. Int. J. Plast. 16 (10–11), 1309–1343.

Rezaee Hajidehi, M., Stupkiewicz, S., 2018. Gradient-enhanced model and its micromorphic regularization for simulation of Lüders-like bands in shape memory alloys. Int. J. Solids Struct. 135, 208–218.

Scalet, G., Niccoli, F., Garion, C., Chiggiato, P., Maletta, C., Auricchio, F., 2019. A three-dimensional phenomenological model for shape memory alloys including two-way shape memory effect and plasticity. Mech. Mater. 136, 103085.

Seupel, A., Hütter, G., Kuna, M., 2018. An efficient FE-implementation of implicit gradient-enhanced damage models to simulate ductile failure. Eng. Fract. Mech. 199, 41–60.

Shaw, J.A., Kyriakides, S., 1995. Thermomechanical aspects of NiTi. J. Mech. Phys. Solids 43 (8), 1243–1281.

Souza, A.C., Mamiya, E.N., Zouain, N., 1998. Three-dimensional model for solids undergoing stress-induced phase transformations. Eur. J. Mech. A Solids 17 (5), 789–806.

Sun, Q.P., Hwang, K.C., 1993. Micromechanics modelling for the constitutive behavior of polycrystalline shape memory alloys—I. Derivation of general relations. J. Mech. Phys. Solids 41 (1), 1–17.

Tanaka, K., 1986. A thermomechanical sketch of shape memory effect: one-dimensional tensile behavior. Res. Mech. 18, 251–263.

Tanaka, K., Nagaki, S., 1982. A thermomechanical description of materials with internal variables in the process of phase transitions. Ing.-Arch. 51 (5), 287–299.

Xu, L., Baxevanis, T., Lagoudas, D.C., 2019. A three-dimensional constitutive model for the martensitic transformation in polycrystalline shape memory alloys under large deformation. Smart Mater. Struct. 28 (7), 74004.

Zhang, M., Baxevanis, T., 2021. An extended three-dimensional finite strain constitutive model for shape memory alloys. J. Appl. Mech. 88 (11).